Time-domain photocurrent spectroscopy based on a common-path birefringent interferometer

[ID] Lukas Wolz, Constantin Heshmatpour, [ID] Antonio Perri, [ID] Dario Polli, [ID] Giulio Cerullo, [ID] Jonathan J. Finley, [ID] Erling Thyrhaug, [ID] Jürgen Hauer, and [ID] Andreas V. Stier
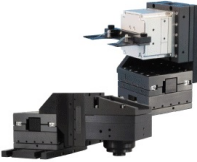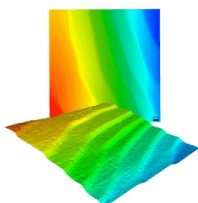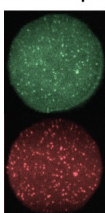
View Online   Export Citation   CrossMark

Nanopositioning Systems

Modular Motion Control

AFM and NSOM Instruments

Single Molecule Microscopes

MCL
MAD CITY LABS INC.
www.madcitylabs.com

Time-domain photocurrent spectroscopy based on a common-path birefringent interferometer

Lukas Wolz,[1] (iD) Constantin Heshmatpour,[2] Antonio Perri,[3,4] (iD) Dario Polli,[3,4] (iD) Giulio Cerullo,[3,4] (iD)
Jonathan J. Finley,[1] (iD) Erling Thyrhaug,[2] (iD) Jürgen Hauer,[2,a] (iD) and Andreas V. Stier[1,b] (iD)

AFFILIATIONS

[1] Department of Physics, Technical University of Munich, Walter Schottky Institut, 85748 Garching, Germany
[2] Dynamical Spectroscopy, Department of Chemistry, Technical University of Munich, 85748 Garching, Germany
[3] IFN-CNR and Dipartimento di Fisica, Politecnico di Milano, Piazza L. da Vinci 32, 20133 Milano, Italy
[4] NIREOS S.R.L., Via G. Durando 39, 20158 Milano, Italy

[a] Juergen.Hauer@tum.de
[b] Author to whom correspondence should be addressed: Andreas.Stier@wsi.tum.de

ABSTRACT

We present diffraction-limited photocurrent (PC) microscopy in the visible spectral range based on broadband excitation and an inherently phase-stable common-path interferometer. The excellent path-length stability guarantees high accuracy without the need for active feedback or post-processing of the interferograms. We illustrate the capabilities of the setup by recording PC spectra of a bulk GaAs device and compare the results to optical transmission data.

Published under license by AIP Publishing. https://doi.org/10.1063/5.0023543

I. INTRODUCTION

Photocurrent (PC) spectroscopy is a key absorption method for the investigation of light–matter interactions and carrier transport in optically active materials.[1,2] The broad range of applications includes characterization of semiconductor band structures,[1,3,4] excitons,[5] and defect bands[6] and the measurement of charge collection efficiency of artificial[7,8] and biological[9] nanoscale devices. Conventionally, PC spectra are recorded in the frequency domain with a tunable (quasi-)monochromatic source. An alternative interferometric implementation is time-domain Fourier Transform (FT) spectroscopy.[10] Time-domain spectroscopy features several advantages over frequency-domain approaches. The most notable in the present context are the well-known Jacquinot[11] and Connes[12] advantage. These state, respectively, that relative to a monochromator-based implementation, an interferometry based spectrometer will have a larger signal-to-noise (S/N) ratio due to increased optical throughput and will feature better wavelength accuracy due to a smaller reliance on accurate optical alignment. In the context of spectroscopy of semiconductor devices and photovoltaics, we also note that interferometer-based spectrometers tend to be

substantially faster, since the collection times are independent of the measured wavelength interval—instead of being purely a function of the desired spectral resolution. While FT photocurrent spectroscopy is advantageous in the infrared spectral range, where light sources are weak and optical features are typically broad, it has been much more difficult to implement in the visible range due to the significantly higher demands for interferometric phase stability. In particular, it is difficult to achieve the desired phase stability of $\lambda/100$ in conventional amplitude division interferometers such as Michelson or Mach–Zehnder geometries. Applications in the visible, based on these designs, thus typically require active phase stabilization or monitoring of path-length fluctuations by co-propagation with a tracer beam. As an alternative to conventional (e.g., Mach–Zehnder) interferometers, we present a photocurrent microscope based on the inherently phase-stable **T**ranslating-**W**edge-based **I**dentical pulses e**N**coding **S**ystem (TWINS)[13] common-path interferometer. Instead of introducing path-length differences for separate replicas, TWINS achieves the desired phase delay τ by the propagation of a single polarized beam through an adjustable amount of birefringent material, resulting in two collinear, orthogonally polarized beams with a precisely controllable relative time delay. The TWINS has

been implemented successfully for bulk samples in several linear and non-linear interferometry applications in the infrared,[14] visible,[15,16] and UV[17] spectral ranges. Furthermore, we recently used it in the demonstration of simultaneous collection of excitation and emission spectra of single molecules.[18] Here, we further extend the versatility of TWINS interferometry by recording spatially resolved time-domain photocurrent spectra in the visible spectral range. As a test sample, we use a simple biased-GaAs photodetector at room temperature. To validate the accuracy of the suggested setup, we compare the photocurrent spectrum retrieved by TWINS to spectra recorded after placing bandpass filters with known properties into the beam path.

II. EXPERIMENTAL SETUP

The TWINS interferometer (NIREOS, model Gemini) has been described in detail elsewhere,[13,19] and here, we only briefly outline its operation principle in Fig. 1(a). An excitation beam is linearly polarized (Pol1) at 45° relative to the optical axis of the birefringent Block A [α-barium borate (α-BBO)]. This results in a pair of equally intense and orthogonally polarized components with a fixed phase delay between them due to the birefringence of the crystal. This phase delay can be compensated with a pair of α-BBO wedges mounted on a linear motorized stage (Block B) as to allow precise control of the effective thickness $d_B(x)$ that the excitation light traverses. Note that the crystal axis of Block B is rotated by 90° with respect to Block A. Thus, after transmission of the two blocks, the total phase delay $\tau(x)$ between ordinary and extraordinary polarization components is

$$\tau(x) = \tau_A - \tau_B(x) = (d_A - d_B(x))\left(\frac{1}{v_{or}} - \frac{1}{v_{ex}}\right), \quad (1)$$

where v_{or} and v_{ex} are the ordinary and extraordinary phase velocities, respectively. Ultimately, the resolution and precision of the interferometer rely solely on the precise movement and range of the wedges. With the typical 100 nm precision of the linear stage, we achieve ~5 attoseconds as phase-delay accuracy at 500 nm and 0.8 ps total phase delay for a scanning range of the wedges of ±12 mm. After passing through the birefringent blocks, Pol2 projects both orthogonal components of the beam into the same polarization state, resulting in the interference of the two polarization components, depending on the total phase delay. The configuration of the TWINS has the following advantages: (*i*) being a common-path instrument, the phase
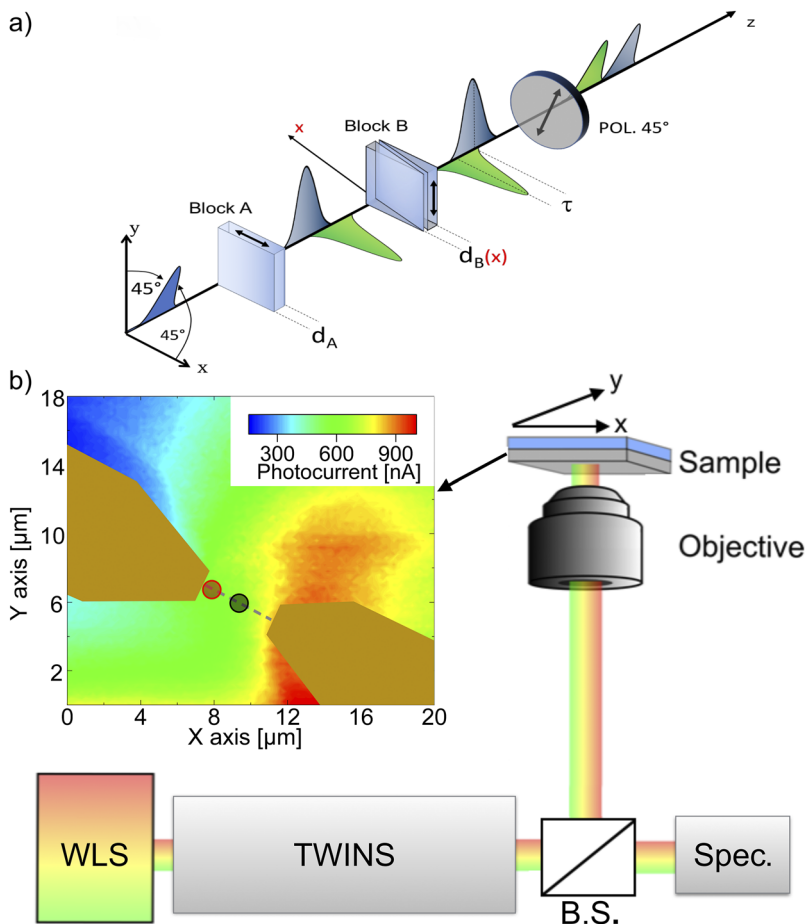

FIG. 1. (a) Illustration of the TWINS interferometer used in this experiment (NIREOS, model Gemini). The excitation light is linearly polarized at Θ = 45°, with respect to the optical axis of the birefringent α-barium borate crystal. Block A induces a fixed phase delay τ_A between the ordinary and extraordinary polarizations. Block B is made of a pair of α-BBO wedges, which can be moved with respect to each other to induce a variable phase delay $-\tau_B(x)$. (b) Schematic of the TWINS photocurrent setup. A white-light source is collimated through the TWINS interferometer and either fiber coupled into a spectrometer or focused (100× objective, *NA* = 0.7) on the photodetector. It consists of a pair of biased gold contacts, evaporated on top of bulk GaAs with a 4 μm gap between them. The photocurrent is detected via two-point measurement by using a Keysight B2912A source meter. The contacts and the spot size are indicated in the PC map. The dashed line indicates a line scan discussed in the text.

delay is—in contrast to, e.g., standard Michelson interferometers—insensitive to mechanical fluctuations, and no feedback stabilization or position tracking is required;[20] (ii) due to the small apex angle of the wedges and the relatively small difference between the refractive indexes of ordinary and extraordinary polarization, the device demultiplies the transverse translation of the wedges, allowing extremely high delay accuracy. The TWINS-photocurrent microscope is schematically shown in Fig. 1(b). As excitation source, the collimated output of a pulsed supercontinuum laser (Fianium, WLS micro, 30 MHz repetition rate) is directed through the TWINS interferometer and focused into a diffraction-limited spot on the photodetector. The total excitation power impinging on the photodetector is estimated by using a silicon-based power meter to be 4 μW–5 μW for all our measurements. The device is mounted on a piezoelectric XYZ stage, allowing (raster) scanning of the sample to yield a spatially resolved photocurrent (PC) map, as illustrated on the left side of Fig. 1(b). The device is connected to a break-out box, and the PC is recorded with a Keysight B2912A source/measure unit (SMU).

III. RESULTS

To demonstrate the scanning microscopy part of the TWINS-PC setup, we measured the photocurrent of a self-made bulk GaAs photodetector, shown in the left side of Fig. 1(b) for a fixed wedge position [$\tau(x) = 0$]. Thus, the PC map is recorded under modulated "white-light" illumination [see Fig. 2(a), wedge position = 0]. The simple GaAs photodetector consists of two gold contacts defined on the surface of the semiconductor using standard e-beam evaporation and optical lithography techniques. The gap between the

contacts was 4 μm, across which a bias voltage (V_{bias}) was applied. The resulting photocurrent as a function of the excitation spot position is shown in the false-color map in Fig. 1(b). Along the indicated line scan, the amplitude of the photocurrent follows the expected potential drop across the contacts (discussed in detail below).

We calibrated the TWINS-PC setup by fiber-coupling the excitation light into a spectrometer (Ocean Optics, HR4000) and recording the spectra for each wedge position. The recorded data for the range of $x = -0.4$ mm to $x = 0.4$ mm are shown in the false-color plot of Fig. 2(a). Clearly, the observed intensity is modulated depending on the wedge position and wavelength. The sinusoidal intensity modulation as a function of wedge position is shown for two wavelengths in Fig. 2(b). As we expect an intensity modulation with a $\lambda/2$-periodicity, the spatial oscillatory period is approximately twice as long for 850 nm as compared to the line cut at 450 nm. Fourier transforming these modulated signals at each wavelength [representative examples shown in Fig. 2(c)] results in a single peak at a pseudofrequency (inverse wedge position, mm^{-1}). A direct correlation between the inverse wedge position and wavelength results in the fully constructed calibration curve shown in Fig. 2(d).

We test the calibration procedure of the setup by measuring the photocurrent spectra of our GaAs detector. With a bias voltage of $V_{bias} = 8$ V, a signal-to-noise ratio of ≈300 was reached, sufficient to demonstrate the capabilities of the herein presented TWINS-PC setup. Figure 3(a) depicts a photocurrent interferogram in the range of −0.4 mm to 0.4 mm. Although the spectrum was recorded over a longer range, the oscillatory signal decays rapidly due to the broad structure of the GaAs absorption spectrum at room temperature. The broad photocurrent spectrum obtained from a Fourier transform of this interferogram is shown
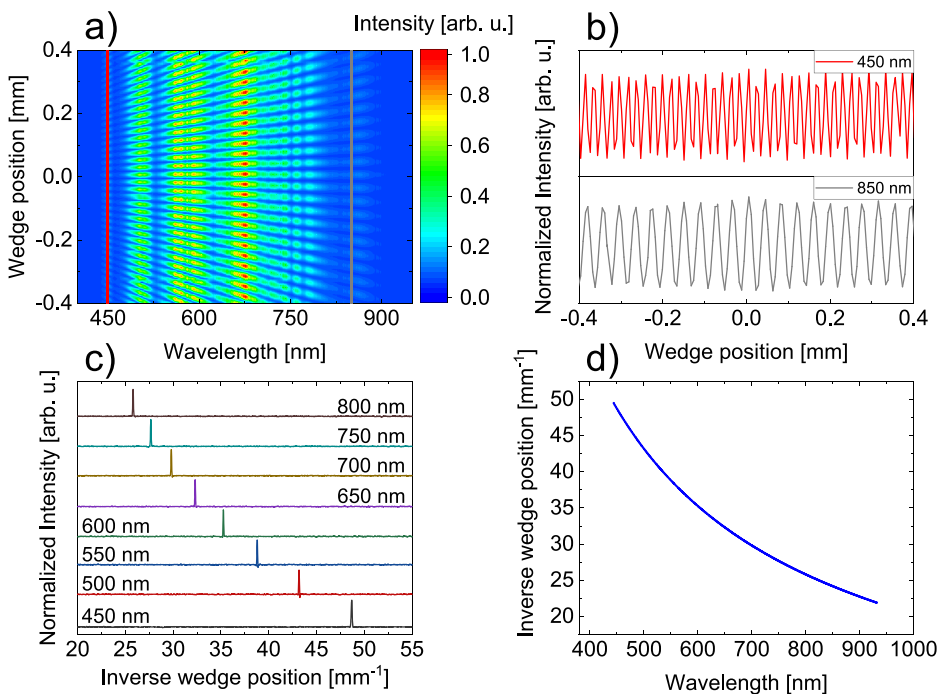

FIG. 2. (a) Color map of the modulated spectral intensity close to zero phase delay [$\tau(x) = 0$]. (b) Vertical line cuts through the spectral intensity shown in (a) at λ = 850 nm and λ = 450 nm, showing the sinusoidal intensity modulation as a function of wedge position. (c) Waterfall plot of the Fourier transforms of the modulated spectral intensity at a variety of fixed wavelengths. The Fourier transform relates the modulation frequency of a specific wavelength to a spatial coordinate linked to the wedge position. (d) Correlation between the measured wavelength and the spatial coordinate obtained from the Fourier transform of the data shown in (a).
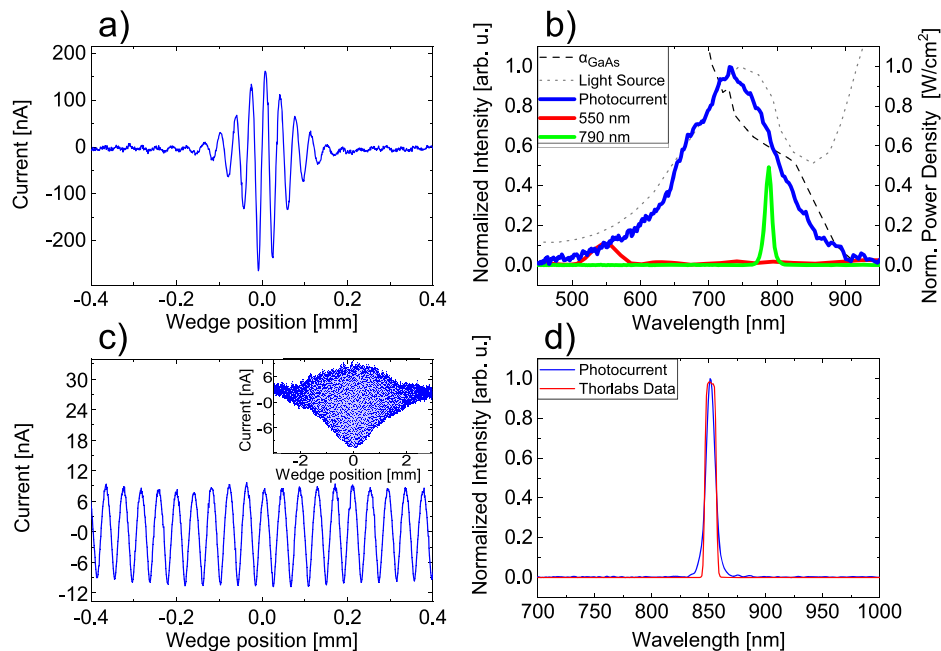
FIG. 3. (a) White-light interferogram of the recorded photocurrent as a function of wedge position in the vicinity of $\tau_A = -\tau_B$. A constant background is subtracted. (b) Fourier-transformed data showing the different photocurrents in the device with respect to the emission wavelength mirroring the spectrum of the incident light on the sample. (c) Interferogram of a bandpass filter centered at 850 nm inserted into the excitation beam path resulting in a high-frequency interferogram. The inset shows the interferogram over the entire scanning range. (d) Comparison of the transmission curve provided by the manufacturer of the bandpass filter (Thorlabs BP850) with the FT of the recorded photocurrent.

in Fig. 3(b). As expected, the signal sets on at the low energy side proportional to the band edge absorption of GaAs (α_{GaAs}, $E_g \approx 1.42$ eV = 875 nm) and cuts off on the high energy side proportional to the intensity of the excitation laser. The insertion of bandpass filters in the excitation beam path artificially limits the spectrum of the illuminating light, which is expected to be visible in the photocurrent spectra. This effect is demonstrated in Figs. 3(b) and 3(c), where we have introduced a variety of bandpass filters spanning the recorded photocurrent spectrum. As expected, the narrow-band excitation is reflected in the narrow-band photocurrent spectra. The interferogram obtained following the insertion of an 850 nm bandpass filter (Thorlabs, FBH850) in the excitation beam path is shown in Fig. 3(c). In the range close to $x = 0$, we obtain the same intensity modulation in the photocurrent as that in the recorded intensity spectra above [Fig. 2(b)]. We compare the Fourier transform of the entire photocurrent interferogram, shown in the inset of Fig. 3(c), with the transmission data obtained from the filter manufacturer in Fig. 3(d) and obtain excellent agreement between the datasets. Specifically, the position and FWHM of both datasets are equal, confirming the calibration procedure and the ability of TWINS–PC to resolve narrow absorption features in this spectral range.

We can compare the presented interferometric photocurrent spectroscopy setup with a wavelength scanning system requiring a monochromator, considering that the minimum number of data points needed to resolve any optical spectra by the two techniques is the same.[21] Namely, if we consider to measure a spectrum with a maximum frequency ν_{max} and a minimum frequency ν_{min} with a desired resolution $\Delta\nu$, the number of samples is equal to $N = \frac{2(\nu_{max} - \nu_{min})}{\Delta\nu}$. The main advantages of the interferometric setup are the throughput advantage and the multiplexing advantage. The former is minimal considering a spatially coherent light source, such as in this case, but can be considerable by using a thermal or LED

radiation. The latter is related to the ability of the interferometric system to excite the sample with all the spectral components simultaneously. Therefore, if we consider an equal number of data points N, the monochromator employs an excitation intensity that is N times lower than that with the TWINS interferometer. By using the TWINS, this results either in lower integration times to achieve the same signal-to-noise ratio or a better signal-to-noise ratio with the same measurement time. The TWINS interferometer has typically a much higher spectral coverage, limited only by the transparency and birefringence of the employed crystals. As an example, the used TWINS interferometer (GEMINI, manufactured by NIREOS) has a working spectral range from 250 nm to 2300 nm in a single device. As the maximum excursion of the birefringent wedges is ±12 mm, the maximum time delay between the pulse replicas is ±0.8 ps, which equates to a maximum resolution of $\Delta\lambda \approx 2$ nm at a wavelength of $\lambda = 700$ nm.[19] Moreover, since no grating is used, the spectral response is much flatter across all the working spectral range. Another important advantage of the presented photocurrent setup is the ability to increase the spectral resolution by simply increasing the scan range of the measurement without affecting the throughput of the system or decreasing the aperture of the device. Employing no entrance or exit slits, the shape of the output beam is constant for all measurement applications. This is especially beneficial if one needs to couple the beam into an optical fiber such as in the presented experimental setup. Since the beam passes through the interferometer without any deviation, the system is easy to align, and the measured spectral properties are less sensitive to misalignment with respect to a grating-based system. Finally, the optical excitation of the sample and, thus, the electronic and vibronic states of the specimen are always constant utilizing the TWINS approach, while in grating spectroscopy, local resonances might be excited unbeknownst to the observer.
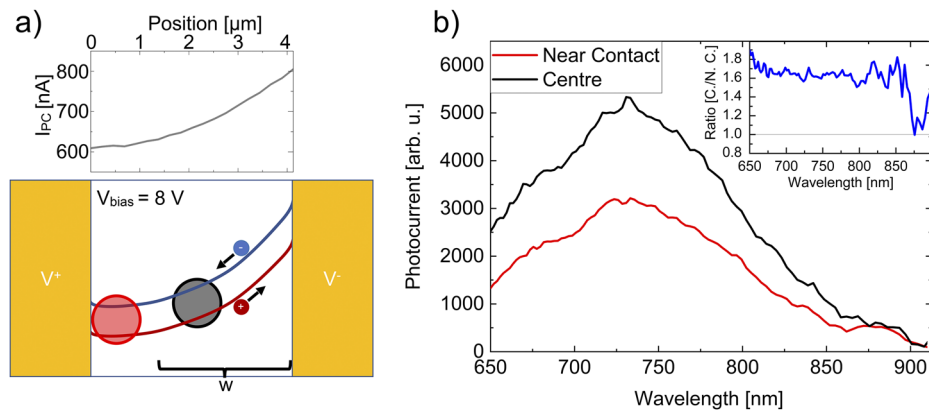
FIG. 4. (a) Top: total photocurrent measured at the fixed wedge position, $x = 0$, when the excitation beam is scanned between the contacts along the gray dashed line shown in Fig. 1(b). Bottom: sketch of the band diagram across the gap between both contacts with applied bias. (b) PC spectra recorded at the positions marked by red and black circles in Fig. 1(b). The overall current detected near the contact is lower in comparison to the current measured in the center. Inset: ratio of the current measured in the center divided by the current obtained near the contact. The ratio is nearly constant for energies well above the GaAs bandgap. Close to the contact, the PCs in the spectral vicinity of the Γ-point of the GaAs bandgap at 875 nm are equal.

Figure 4(a) shows the photocurrent at a fixed wedge position, $x = 0$, recorded while the excitation beam is scanned along the gray dashed line shown in Fig. 1(b). We observe a monotonically increasing photocurrent from the positive contact toward the negative contact, as expected. Below, we sketch the related band diagram of our illuminated undoped GaAs sample ($N_D \sim 10^{15}$ cm^{-2}). For a bias voltage of $V_{bias} = 8$ V, the depletion region w is ~2 μm to 3 μm wide, indicating that close to the positive contact, flat bands are expected. We highlight the photocurrent spectra at two positions, close to the positive contact and in the middle of the gap between the contacts, as indicated in Fig. 1. The total photocurrent signal represents the sum of competing mechanisms such as drift currents under the influence of an electric field that depend on carrier lifetime and mobility, diffusion currents that depend on overall generation rate, resident carrier density, and photothermal effects.[1] We expect that close to the positive contact, where the bands are flat, the dominating drift current to be smaller as compared to regions where band bending effects occur in the semiconductor. This is shown in Fig. 4(b), where we plot the PC spectra measured at both positions. The overall current measured in the center between the contacts is higher compared to the current obtained near the contact, reflecting the stronger dependence of the drift currents on the electric field. The ratio (center/near contact) of both currents is plotted in the inset. For higher energies, this ratio is constant ~1.6 to 1.7. However, in the spectral vicinity of the Γ-point of the GaAs bandgap, the relative strengths of the PCs that were recorded are equal. This measurement exemplifies the capability of our setup for PC spectroscopic mapping combining high spatial and spectral resolutions.

IV. CONCLUSION AND OUTLOOK

To conclude, we have experimentally validated broadband diffraction-limited photocurrent microscopy following visible excitation. Use of a TWINS birefringent interferometer allows for photocurrent spectroscopy. The TWINS was calibrated by using a standard grating-based spectrometer. We further verified the calibration of the TWINS–PC device by performing photocurrent measurements with narrowband excitation selected by a series of interference filters and comparing the retrieved spectra with tabulated ones. Due to the intrinsic phase stability of TWINS, the spectrometer achieves high accuracy without the need for active feedback or path-length tracking, bringing some of the advantages of FT spectroscopy down to the visible spectral region. For our proof of principle experiments here, we achieved an S/N ratio of ≈300. Data averaging and lock-in detection schemes may be employed easily to significantly improve the S/N. We discussed several advantages of the presented technique as compared to a common wavelength scanning system with a monochromator. TWINS can reduce the measurement times and increase the working spectral range considerably. Finally, as reported previously, TWINS can be employed for time-resolved measurements using ultrashort pulses after minor modifications to the interferometer design,[15] highlighting the versatility of this approach.[22–24]

AUTHORS' CONTRIBUTIONS

L.W. and C.H. contributed equally to this work.

DATA AVAILABILITY

The data that support the findings of this study are available from the corresponding author upon reasonable request.

REFERENCES

[1] S. M. Sze and K. K. Ng, *Physics of Semiconductor Devices* (John Wiley & Sons, 2006).

[2] J. Nelson, *The Physics of Solar Cells* (World Scientific Publishing Company, 2003).

[3] G. Bastard, *Wave Mechanics Applied to Semiconductor Heterostructures* (Halsted Press, 1988).

[4] K. F. Mak, C. Lee, J. Hone, J. Shan, and T. F. Heinz, "Atomically thin MoS_2: A new direct-gap semiconductor," Phys. Rev. Lett. **105**(13), 136805 (2010).

[5] A. R. Klots *et al.*, "Probing excitonic states in suspended two-dimensional semiconductors by photocurrent spectroscopy," Sci. Rep. **4**, 6608 (2014).

[6] M. Vanecek and A. Poruba, "Fourier-transform photocurrent spectroscopy of microcrystalline silicon for solar cells," Appl. Phys. Lett. **80**(5), 719–721 (2002).

[7] Z. Xiao, Q. Dong, C. Bi, Y. Shao, Y. Yuan, and J. Huang, "Solvent annealing of perovskite-induced crystal growth for photovoltaic-device efficiency enhancement," Adv. Mater. **26**(37), 6503–6509 (2014).

[8] M. Blauth, G. Vest, S. L. Rosemary, M. Prechtl, O. Hartwig, M. Jürgensen, M. Kaniber, A. V. Stier, and J. J. Finley, "Ultracompact photodetection in atomically thin $MoSe_2$," ACS Photonics **6**(8), 1902–1909 (2019).

[9] S. C. Feifel, K. R. Stieger, H. Lokstein, H. Lux, and F. Lisdat, "High photocurrent generation by photosystem I on artificial interfaces composed of π-system-modified graphene," J. Mater. Chem. A **3**(23), 12188–12196 (2015).

[10] S. P. Davis, M. C. Abrams, and J. W. Brault, *Fourier Transform Spectrometry* (Academic Press, 2001).

[11] M. R. Descour, "Throughput advantage in imaging Fourier-transform spectrometers," Proc. SPIE **2819**, 285–290 (1996).

[12] P. R. Griffiths, C. T. Foskett, and R. Curbelo, "Rapid scan infrared Fourier transform spectroscopy," Appl. Spectrosc. Rev. **6**(1), 31–77 (1972).

[13] A. Oriana, J. Réhault, F. Preda, D. Polli, and G. Cerullo, "Scanning Fourier transform spectrometer in the visible range based on birefringent wedges," J. Opt. Soc. Am. A **33**(7), 1415–1420 (2016).

[14] J. Réhault, M. Maiuri, C. Manzoni, D. Brida, J. Helbing, and G. Cerullo, "2D IR spectroscopy with phase-locked pulse pairs from a birefringent delay line," Opt. Express **22**(8), 9063–9072 (2014).

[15] J. Réhault, M. Maiuri, A. Oriana, and G. Cerullo, "Two-dimensional electronic spectroscopy with birefringent wedges," Rev. Sci. Instrum. **85**(12), 123107 (2014).

[16] F. Preda, A. Oriana, J. Réhault, L. Lombardi, A. C. Ferrari, G. Cerullo, and D. Polli, "Linear and non-linear spectroscopy by a common-path birefringent interferometer," IEEE J. Sel. Top. Quantum Electron. **23**(3), 88–96 (2017).

[17] R. Borrego-Varillas, A. Oriana, L. Ganzer, A. Trifonov, I. Buchvarov, C. Manzoni, and G. Cerullo, "Two-dimensional electronic spectroscopy in the ultraviolet by a birefringent delay line," Opt. Express **24**(25), 28491–28499 (2016).

[18] E. Thyrhaug, S. Krause, A. Perri, G. Cerullo, D. Polli, T. Vosch, and J. Hauer, "Single-molecule excitation–emission spectroscopy," Proc. Natl. Acad. Sci. U. S. A. **116**(10), 4064–4069 (2019).

[19] A. Perri, F. Preda, C. D'Andrea, E. Thyrhaug, G. Cerullo, D. Polli, and J. Hauer, "Excitation-emission Fourier-transform spectroscopy based on a birefringent interferometer," Opt. Express **25**(12), A483–A490 (2017).

[20] T. Zhang, C. N. Borca, X. Li, and S. T. Cundiff, "Optical two-dimensional Fourier transform spectroscopy with active interferometric stabilization," Opt. Express **13**(19), 7432–7441 (2005).

[21] P. R. Griffiths and J. A. De Haseth, *Fourier Transform Infrared Spectrometry* (John Wiley & Sons, 2007), p. 16.

[22] N. Zhou, Z. Ouyang, J. Hu, O. F. Williams, L. Yan, W. You, and A. M. Moran, "Distinguishing energy- and charge-transfer processes in layered perovskite quantum wells with two-dimensional action spectroscopies," J. Phys. Chem. Lett. **11**(12), 4570–4577 (2020).

[23] P. Gregoire, A. R. S. Kandada, E. Vella, C. Tao, R. Leonelli, and C. Silva, "Incoherent population mixing contributions to phase-modulation two-dimensional coherent excitation spectra," J. Chem. Phys. **147**(11), 114201 (2017).

[24] K. J. Karki, J. R. Widom, J. Seibt, I. Moody, M. C. Lonergan, T. Pullerits, and A. H. Marcus, "Coherent two-dimensional photocurrent spectroscopy in a PbS quantum dot photocell," Nat. Commun. **5**, 5869 (2014).